Pulse-shape-dependent strong-field ionization viewed with velocity-map imaging

Dominik Geißler, Tamás Rozgonyi, Jesús González-Vázquez, Leticia González, Philipp Marquetand, and Thomas C. Weinacht

Phys. Rev. A **84**, 053422 — Published 17 November 2011

DOI: 10.1103/PhysRevA.84.053422

Pulse Shape Dependent Strong Field Ionization Viewed with Velocity Map Imaging

Dominik Geißler,[1] Tamás Rozgonyi,[2] Jesús González-Vázquez,[3]
Leticia González,[4] Philipp Marquetand,[4] and Thomas Weinacht[1]

[1] *Department of Physics, Stony Brook University, Stony Brook, New York 11794 USA*
[2] *Chemical Research Center of the Hungarian Academy of Sciences, P.O. Box 17, Budapest 1525, Hungary*
[3] *Instituto de Química Física Rocasolano, CSIC, C/Serrano 119, 28006 Madrid, Spain*
[4] *Friedrich-Schiller-Universität Jena, Institut f. Physikalische Chemie, Helmholtzweg 4, 07743 Jena, Germany*

We explore strong field molecular ionization with velocity map imaging of fragment ions produced by dissociation following ionization. Our measurements and *ab initio* electronic structure calculations allow us to identify various electronic states of the molecular cation populated during ionization, with multiple pathways to individual states highlighted by the pulse shape dependence. In addition we show that relative populations can be reconstructed from our measurements. The results illustrate how strong field molecular ionization can be complicated by the presence and interaction of multiple cationic states during ionization.

PACS numbers:

I. INTRODUCTION

Strong field ionization of molecules has drawn considerable attention in the past few years. It has been used to image molecular orbitals [1, 2], and it is a necessary first step in the generation and detection of attosecond electron dynamics [3, 4]. The recollision of an electron wave packet with the atomic or molecular core after strong field ionization gives rise to attosecond light pulses, which can be used to capture the motion of electrons in the atom or molecule being ionized, or a subsequent system upon which the attosecond pulses are incident [5]. While the understanding of atomic ionization has become quite detailed [6], there are still many aspects of molecular ionization which are not understood. For example, the role of electron correlation and Koopmans correlations between initial neutral states and final cationic states is still not understood [7], with new calculations aiming to address this [8]. Our focus here is on the superposition of electronic states of the molecular cation generated by ionization in a short, intense laser pulse [9–13]. While such superpositions have been discussed in the context of high harmonic generation [2, 14–16], we make use of velocity map imaging and *ab initio* electronic structure calculations to characterize the superposition of cationic states or 'electron holes' generated via strong field ionization.

In an earlier publication, we used pump probe spectroscopy, with a shaped pump pulse to demonstrate the superposition of several bound cationic states in CH_2I_2 [10]. In this article, we focus on dissociative electronic states of CH_2BrI^+ that result in the breaking of the C-I bond in the cation, leading to the production of CH_2Br^+. This fragment dominates the time of flight mass spectrum and comes from ionic states that correspond to removing an electron from deeper molecular orbitals, rather than just the HOMO or HOMO−1. We measure the velocity distribution of CH_2Br^+ fragments as a function of pulse shape and interpret the measurements with the help of *ab initio* electronic structure calculations of the parent and fragment cations.

II. EXPERIMENTAL SETUP AND DATA ACQUISITION

The laser system is described elsewhere in detail [17]. In brief, we use a Kerr Lens modelocked Titanium Saphhire oscillator to seed a multi-pass amplifier, which generates near transform-limited laser pulses with a pulse duration of 30fs centered around 780nm at a repetition rate of 1kHz. The maximum pulse energy is about 1mJ. The experiments described in this paper are performed using a single beam apparatus, with the pulse shapes and sequences (chirped pulses and pump-probe scans) generated by an acousto-optic modulator (AOM) based ultrafast pulse shaper [18]. For the chirp based experiments we varied the second-order phase of the pulse between -2000 fs^2 and +2000 fs^2 and kept the ion yield per pulse roughly constant, entailing an increase in the pulse energy from an unshaped pulse to the maximum or minimum chirp of about 1.6. For experiments where we studied the ion yield as a function of intensity, the pulse shaper was used to automatically change the intensity while the ion yields were recorded and transferred to the computer. The peak intensity was varied between $1.7 \cdot 10^{13}$ W cm^{-2} and $5.7 \cdot 10^{13}$ W cm^{-2} for transform-limited pulses. In a series of measurements aimed at identifying multiple pathways to a given ionic final state, we programmed our pulse shaper to produce two pulses ('pump' and 'probe') with fixed relative phase but variable delay. For the pump probe experiment the intensities of the two pulses were $3.9 \cdot 10^{13}$ W cm^{-2} and $7.2 \cdot 10^{12}$ W cm^{-2} for the pump and probe pulses respectively.

The laser pulses interact with the target molecule CH_2BrI in a molecular beam chamber with the background pressure being about 10^{-6} Pa. All results discussed in this paper are based on ions detected after interaction with the laser pulses. We use a velocity map imaging setup, which allows one to measure the ion masses, and their momentum along two dimensions. The momentum space of the ions at their point of ionization is mapped into the position space at the surface of the

detector, using several electrostatic lenses. The setup is similar to the one described in [19]. The ion signal is measured by a position-sensitive micro-channel plate (MCP) and phosphor screen and then captured and digitalized by a camera. The MCPs are gated and allow us to select specific molecular fragment ions by switching them on only around the arrival time of the fragment of interest. In addition to velocity map imaging mode, the apparatus can be configured to operate as a traditional time of flight spectrometer, by switching off the MCP gating and reading the time-of-flight signal from the phosphor screen through a highpass filter.

The molecular gas in the vacuum chamber was at room temperature and thus the measured momentum distributions are broadened by the motion of the molecules prior to their interaction with the laser. The calibration of position on the phosphor screen to ion momentum vector/energy was performed by creating a detailed model of our velocity map imaging spectrometer using the Simion software package [20]. As this paper discusses changes in the momentum distribution of fragment ions, special care was taken to avoid systematic errors in the ion detection, most notably space charge (the mutual repulsion ions feel when created close to each other in the laser focus) and an inhomogeneous detector efficiency. While our measurements were made at molecular beam densities such that multiple ions were collected for each laser shot, we checked our pulse shape dependent velocity map imaging (VMI) measurements against measurements made with low molecular beam densities to ensure that changes in the velocity distribution were not due to space charge (which can change the velocity distribution for varying total ion yields). The second detector related issue is that MCP detectors typically develop a non-uniform sensitivity to ions with usage, leading towards a lower count rate for ions hitting less sensitive areas of the MCP. In our case, the MCPs have degraded close to the center. To circumvent this problem, a sensitivity map of the detector was measured and used to correct for the sensitivity bias. The map was created by blurring the ion lens and measuring hydrogen ions only, as we expect this to yield a uniform momentum distribution. We estimate that our corrections for non-uniform detection sensitivity leave a maximum error of 2% in the measured kinetic energy release (KER) distributions.

III. CALCULATIONS

In order to interpret the experimental results, we performed quantum-chemical and quantum-dynamical calculations. The geometries for the neutral and ionic parent molecule (CH_2BrI and CH_2BrI^+) as well as CH_2Br^+ were optimized by density functional theory with the help of the Gaussian03 package of programs [21] using the B3LYP functional [22, 23] with the aug-cc-pVTZ basis set [24] for H, C and Br atoms and the aug-cc-pVTZ-PP basis set for the I atom. The normal mode vibrational coordinate of the parent cation in its ground electronic state was also determined with the same method. As pointed out in previous publications [25, 26], strong field ionization of CH_2BrI by a near infrared (IR) ∼30 fs laser pulse induces a vibrational wave packet in the I-C-Br bending mode in the ground electronic state of CH_2BrI^+. With a simple one-dimensional model, we were able to describe the time-dependent formation of CH_2Br^+ by a probe pulse as the wave packet oscillates on the ground ionic state surface and comes into resonance with higher lying dissociative states [26]. In this model, the potential energy curves for the lowest five ionic states and for the ground state of the neutral molecule along the I-C-Br bending normal mode coordinate, u, were computed with the state-averaged complete active space self-consistent field (SA-CASSCF) method [27] with the Molcas 7.2 program package [28]. The active space consisted of 8 orbitals with 11 and 12 electrons for the ionic and for the neutral molecule respectively, and included the bonding and antibonding carbon-halogen orbitals and the lone pairs on the halogen atoms. Transition dipole moments (TDM) and spin-orbit couplings (SOCs) among the ionic states were also determined and used in the dynamical simulations. The ionic potential curves are presented in figure 1. For further details of the model see reference [26].

In order to estimate the available fragment ion kinetic energies from different ionic states, we first determined the excitation energies of the parent cation at the equilibrium geometry of the neutral molecule. We label this Franck-Condon point FC_1, in order to differentiate it from other Franck-Condon points defined below. Afterwards, we calculated the excitation energies of CH_2Br^+. These calculations were performed with the more accurate multireference configuration interatcion (MRCI) method using the Molpro program package [29]. Here we used the same (11,8) active space for the parent ion as before, but now we included 18 doublet and 9 quartet states into the computation. SOCs were taken into consideration with [30, 31]. Excitation energies for CH_2Br^+ were computed with an active space of 7 electrons and 5 orbitals involving 5 singlet and 5 triplet states for the ionic fragments in the computations. For both the SA-CASSCF and MRCI computations, the Douglas-Kroll Hamiltonian and the ANO-RCC basis sets [32, 33] with contractions equivalent to the triple zeta plus polarization type basis were used. The MRCI excitation energies for CH_2Br^+ were then combined with available experimental data (i.e. experimental values are used when available): the ionization potential (9.692 eV) of CH_2BrI [34], the appearance energy (10.813 eV) of CH_2Br^+ [34], and the SO-splitting (0.94 eV) of neutral iodine [35]. The resulting energies with respect to the ground state energy of the parent ion at the FC_1 geometry are shown in figure 1.

Excitation energies of CH_2Br^+ were determined for different geometries - optimized for different multiplicities of the same fragment by DFT - depending on which ge-

ometry gives the lowest excitation energy. That is, the energy of the ground state CH_2Br^+ fragment belongs to a geometry optimized for the singlet ground state, while the energies of the excited CH_2Br^+ fragment were obtained for a geometry optimized for the lowest triplet state.

We note that FC'$_1$ (see figure 1), which is the minimum energy point on the neutral potential along the bending normal coordinate of the cation, is slightly different from the real Franck-Condon point, FC_1. This, together with the difference in the applied level of theory (SA-CASSCF versus MRCI) results in a minor difference in the ionic excitation energies seen in figure 1 at FC'$_1$ and at FC_1. This minor difference does not influence the theoretical interpretation of the present experimental observations.

The quantum dynamics were treated as in [26], by solving the time-dependent Schrödinger equation, with the explicit treatment of the time-dependent laser-molecule interaction in the dipole approximation. A complete description of the strong field ionization (as developed in [8]) is beyond the scope of this article, and therefore we developed a simple model in order to capture the effects of vibrational dynamics and electronic resonances during ionization. We modeled the strong field ionization process as an interaction of the molecule with two superimposed pulses: a weak EUV pulse whose photon energy was tuned to couple the ground state of the neutral molecule to a particular ionic electronic state, and a strong IR laser pulse with the experimental photon energy (1.58 eV), which coupled the first five ionic states. In order to account for the strong intensity dependence of the multi-photon ionization, we used a 20 fs EUV pulse instead of the experimental 40 fs FWHM for the ionizing pulse, although we note that our calculations were not very sensitive to the duration of the EUV pulse. In order to avoid unphysical Rabi-oscillation between the ionic and neutral states in the model, we used a small pulse area (integral of the Rabi frequency) for the ionizing pulse, while we used the experimental peak field strength for the transform-limited 1.58 eV pulse. As dynamic Stark shifts may shift the ionic levels considerably at this intensity, the resonant neutral-to-ionic frequencies for each ionic state were chosen by scanning the frequency of the ionizing EUV pulse in the presence of the strong 1.58 eV electric field. The 1.58 eV pulse was chirped, with the peak intensity chosen to match the experimental values, and the asymptotic populations in the different ionic excited states of the model were determined as a function of the linear chirp parameter.

Previous dissociative photoionization experiments [34] indicate that complete dissociation is expected when the energy absorbed from the laser pulse is larger than the dissociation limit and that the main photoproduct is CH_2Br^+ for energies up to 3 eV above the dissociation limit. Therefore, in the dynamics simulations we regard the asymptotic population of electronic states above the dissociation limit as the CH_2Br^+ ion yield.

The calculations described above allow us to identify

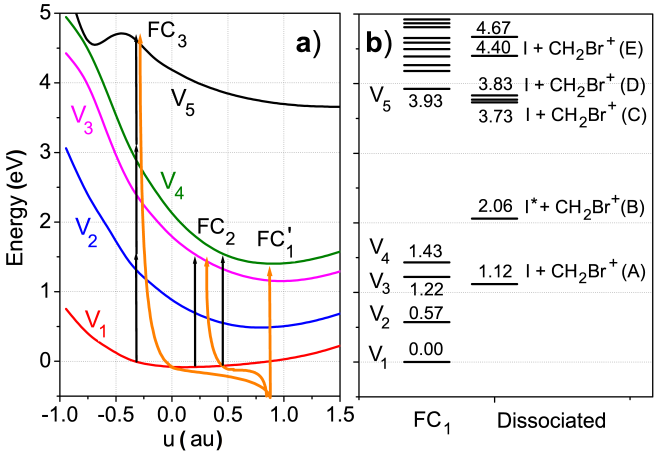

FIG. 1: These graphs summarize the results from the calculations described in section III. Panel a (based on SA-CASSCF computations) shows the energy of the five lowest adiabatic states of CH_2BrI^+ along the bending normal mode coordinate u. The black arrows indicate the position of several FC points - FC_1 for vertical ionization from the neutral ground state, FC_2 for the close lying V_1/V_3, V_1/V_4 resonances, and FC_3 for the three photon V_1/V_5 resonance. Panel b (based on MRCI combined with experimental values) shows the minimum electronic energy of the first few ionic states (left column) and the minimum electronic energy required to create CH_2Br^+ in various electronic states: A, B, C, D and E.

different possible dissociation pathways and make predictions regarding the kinetic energy release for each channel. Figure 1 shows that V_3 (mainly corresponding to the removal of an electron from a lone pair orbital on Br) is the lowest electronic state leading towards dissociation (channel A). Molecules which are ionized directly to V_3 without passing through lower ionic states (i.e. vertical ionization at FC_1) will be referred to as 'direct V_3'. Taking the difference between the energy available at FC_1 on V_3 and the asymptotic state (channel A), yields an upper limit for kinetic energy released during dissociation after direct ionization to V_3 of 100 meV. The state V_4 (also corresponding to a singly occupied lone pair of Br) is energetically very close. Population created there in a similar way by ionization at FC_1, will be referred to as 'direct V_4' and has a maximum KER of 310 meV via channel A. However, as figure 1 indicates, in addition to direct vertical ionization to V_3 and V_4, ionization to these states can also proceed indirectly via V_1. Ionization to V_1 on the leading edge of the pulse can be accompanied by wave packet evolution on V_1 to locations where V_3 and V_4 are resonant with V_1 and are thus efficiently populated by the tail of the pump pulse. The resonance locations are labeled FC_2, as the two FC points (to V_3 and V_4) are very close and cannot be resolved by our experiment). This indirect ionization process will be referred to as 'indirect V_3 and V_4', and according to the calculations, should lead to a maximum KER of 460 meV (channel A, indirect V_3 and V_4). While we cannot distinguish indirect V_3 from

indirect V_4 since they have the same total energy, the calculations indicate that indirect V_4 dominates.

Ionizing to V_5 (whose configuration corresponds to a hole in a bonding C-I orbital) can also lead to the production of CH_2Br^+. Excitation to V_5 can take place either directly (vertical ionization), or indirectly via V_1 at FC_3. Direct ionization to V_5 can lead to CH_2Br^+ with four different dissociation channels being energetically accessible (A, B, C and D), leading to KERs of 2.81 eV, 1.87 eV, 200 meV and 100 meV respectively. Molecules excited indirectly to V_5 have several possible dissociation channels resulting in KERs from a few hundred meV (E and above) to 3.62 eV (A). We note that we do not measure many ions with a KER between 1 eV and 2 eV, suggesting that channel B (with a KER of 1.87 eV) is not favored from V_5. It should also be mentioned that fragment ions can also be formed from dissociating neutral states (ion pair states), by creating negative and positive ions. We did not observe any negative ions with the pulse shapes used for this paper, and thus we do not take these states into consideration.

IV. EXPERIMENTAL RESULTS AND DISCUSSION

Figure 3 shows a typical two-dimensional momentum distribution of CH_2Br^+ after single pulse excitation. As the creation of each CH_2Br^+ ion from CH_2BrI is essentially a two body process (neglecting electron recoil and drift in the electromagnetic field), measuring the momentum of either fragment allows us to determine the total kinetic energy release for this process. Since the calculations yield dissociation energies for different dissociation channels, we will discuss the ion yield as a function of KER, $Y(E)$, rather than momentum or velocity. We note that in order to highlight features in the measurements at higher KER (which are important for discriminating between different states and pathways) we have not included the Jacobian in transforming the x axis from momentum to energy - i.e. we have only rescaled the x axis in going from momentum to energy. During dissociation some of the available energy can also be invested in rotational, vibrational and electronic degrees of freedom of the fragments; these cannot be directly measured with our apparatus. Furthermore, we note that in addition to the calculations having an uncertainty on the order of 100 meV, we also expect that thermal energy stored in the multiple molecular degrees of freedom prior to ionization and dynamic Stark shifts due to the strong field laser pulse during ionization can lead to high energy tails in the measured KER. Dissociative photoionization measurements indicate that up to 100-200 meV of internal energy can go towards dissociation [34]. Calculations of dynamic Stark shifts associated with field strengths of 6 GV/m can be a few hundred (*ca.* 300) meV [26], although only a small fraction of the Stark shift energy is expected to show up in the KER, given that the wave packet on the Stark shifted PES will only move a short distance (over which the Stark shift does not change much) during the duration of the laser pulse.

In addition to measuring KER, it is useful to distinguish dissociation channels and initial states by the energy dependent angular distribution. For this purpose the complete fragmentation pattern was divided into two sectors, as indicated with the dashed black lines in figure 2: A "parallel sector", which restricts the radial integral to ± 45 deg and 180 deg ± 45 deg, i.e. ions which are ejected rather along the laser polarization, and an "orthogonal sector" which only counts ions ejected orthogonally to the laser polarization axis (i.e. at 90 deg ± 45 deg and 270 deg ± 45 deg). Based on the "orthogonal" $Y_o(E)$ and the "parallel" $Y_p(E)$ ion count, an asymmetry parameter, $A(E)$, versus kinetic energy release was calculated as $\frac{Y_p(E)-Y_o(E)}{Y_p(E)+Y_o(E)}$.

It is natural to suspect that each ionic state will lead to a different distribution of KER via the different possible dissociation channels. For this reason, the KERs for different ionic states can overlap and higher lying states can even lead to lower KER than lower lying states. Therefore, it is difficult to assign the different features in the VMI spectrum for a single unshaped laser pulse to specific states without additional information. Hence, we measured the VMI spectrum for several key pulse parameters (pulse intensity, second-order phase and double pulses) in order to resolve additional structure and to establish a clear relationship between features in the VMI spectrum and excitation pathways to several cationic states of the molecule.

A. Single Pulse Analysis - Intensity Scans

As a starting point in disentangling different processes that lead to CH_2Br^+, we studied the momentum resolved fragment ion yield versus pulse intensity. We ionized the molecules with transform-limited pulses (Gaussian temporal profile, minimum duration) having a peak intensity ranging from $2.0 \cdot 10^{13}$ W cm^{-2} to $3.9 \cdot 10^{13}$ W cm^{-2}. Figure 3 shows the integrated radial lineouts for CH_2Br^+ taken at two different intensities close to the two extrema of the intensity range studied. As shown in this figure, the energy distributions have a generic double peak structure, with a "slow peak" centered at 50 meV and "fast peak" centered at 2.6 eV. Interestingly, there are no further structures for higher KER; no ions were observed beyond the "fast" peak up to the limit of our detector, which is about 12.6 eV.

While the ion yields at different KER within each peak scale similarly with intensity, the total ion yields for the two peaks scale differently with intensity. The fast/slow ratio converges to zero in the limit of weak excitation intensities, as can be seen in the low intensity graph in figure 3. At relatively low intensities, one expects the production of fragment ions to be dominated by the lowest dissociative state of the cation (see [34]), which is

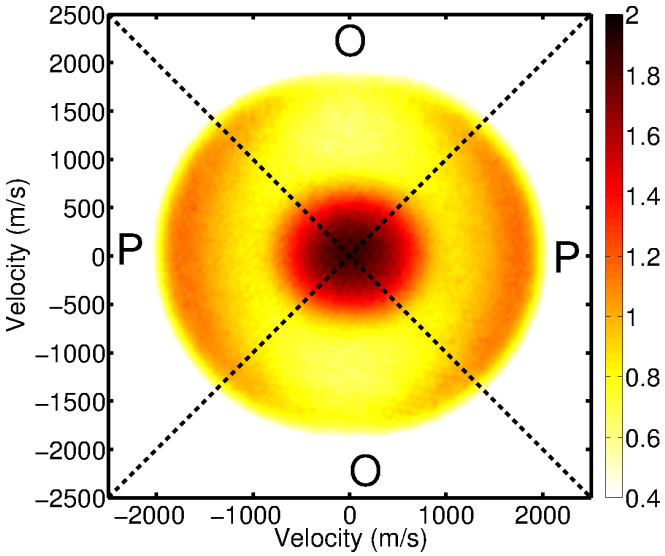

FIG. 2: 2D velocity distribution of CH_2Br^+ for a single unshaped laser pulse. The color axis represents the ion yield on a logarithmic scale. The x and y axis show the velocity along the x and y direction of the detected ions. The laser polarization was along the y-axis. The sample was prepared at room temperature and was not oriented. One can clearly see that the total ion yield can be sorted into a slow and fast group of ions. Also the fast group exhibits a strong tendency to be ejected along the laser polarization. The dashed black lines indicate the borders between the parallel (P) and the orthogonal sectors (O).

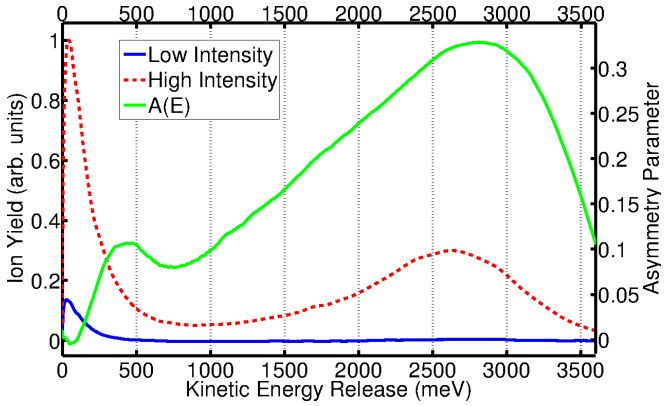

FIG. 3: This graph shows two typical KER distributions of CH_2Br^+ fragments. The solid blue (black) curve was taken at low intensity ($2.0 \cdot 10^{13}$ W cm^{-2}), while the dotted red (gray) curve corresponds to high laser intensity ($3.9 \cdot 10^{13}$ W cm^{-2}). The solid green (light gray) curve shows the asymmetry parameter versus KER for the dotted red curve. The total kinetic energy release was calculated based on the measured CH_2Br^+, assuming a two body dissociation process.

V_3. Since ionization to V_5 would require the absorption of at least 2 additional photons, the fact that the slow peak changes uniformly with intensity over a range of intensities where the fast/slow ratio changes dramatically (between $\sim 2 \cdot 10^{13}$ W cm^{-2} and $4 \cdot 10^{13}$ W cm^{-2}) suggests that direct ionization to V_5 does not contribute to the slow peak, despite the energetically accessible channels C and D. Out of the different possible excitation pathways discussed in section III, the direct V_3, V_4, and the indirect V_3, V_4 populations match our observations of the slow peak. In addition to the fact that they are separated by a sufficiently small amount such that they are expected to show a similar intensity dependence, their predicted cutoff energies (100 meV for direct V_3, 310 meV for direct V_4, and 460 meV for indirect $V_{3,4}$) for the KER are close to the cutoff of the slow peak (which extends to about 500 meV). While population of V_3 and V_4 during ionization can explain the ions measured in the slow peak, the predicted cutoff energies are well below the slow shoulder of the fast peak. For this reason, populating V_3 and V_4 cannot contribute to the fast peak. As will be discussed later (section IV B and IV C), varying the pulse shape allows one to disentangle and control the direct and indirect contributions to the slow peak.

As the fast peak appears with increasing intensity, ionization to the next excited state, V_5, is the natural assignment for the fast peak. The electron configuration for V_5 corresponds to a hole in the σ(C-I) bonding orbital, and the maximum expected KER for V_5 is 2.82 eV, which can explain most ions of this peak. Additionally, the intensity scaling implies that only V_5, or states which are very close by, contribute to the fast peak. After V_5, the next few states have mostly quartet character, and we do not expect substantial population of these via ionization of the singlet ground state. The first excited doublet state after V_5 corresponds to a single occupied σ (bonding) C-Br orbital. Therefore, ionization to this state is expected to lead predominantly to CH_2I^+, and we thus assign the fast peak in the CH_2Br^+ KER spectrum to V_5.

B. Pump-Probe Parameterization

In order to search for indirect contributions to excited ionic states, we studied the CH_2Br^+ KER for a pump-probe pulse shape parameterization, where the pulse shaper was used to generate two Gaussian pulses (pump and probe) and their time-separation was varied. Figure 4 shows the CH_2Br^+ ion yield $Y(t, E)$ versus KER, E, and pump probe time delay, t. In this section we demonstrate how the KER distributions associated with the indirect populations $V_{3,4}$ and V_5 can be reconstructed. Furthermore, we use these reconstructed KER distributions to extract the time-dependent indirect populations. They are shown in figure 5, as the green/lower light gray curve (indirect $V_{3,4}$) and the red/upper dark gray curve (indirect V_5). The total signal of the fragment and the parent ion, are shown as the light/dark blue (upper light gray/lower dark gray) graph in figure 5. As discussed in [25], modulations in the various ion yields versus time delay can be interpreted as ionization to V_1, by the pump followed by transfer to $V_{3,4}$ (where the molecule disso-

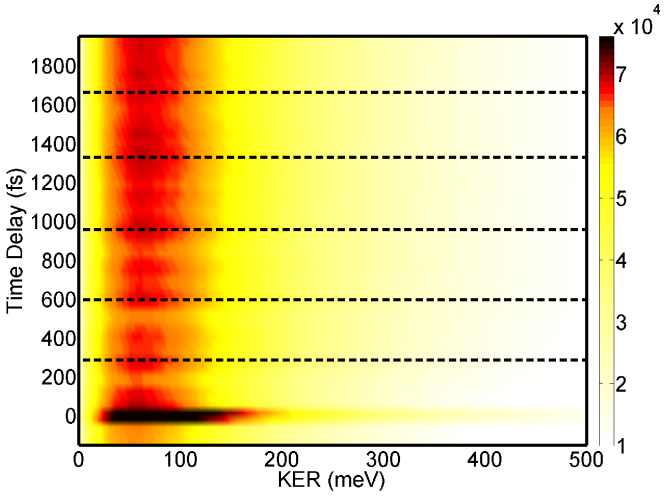

FIG. 4: CH_2Br^+ yield versus KER and pump-probe time delay, $Y(t, E)$, summed over both sectors.

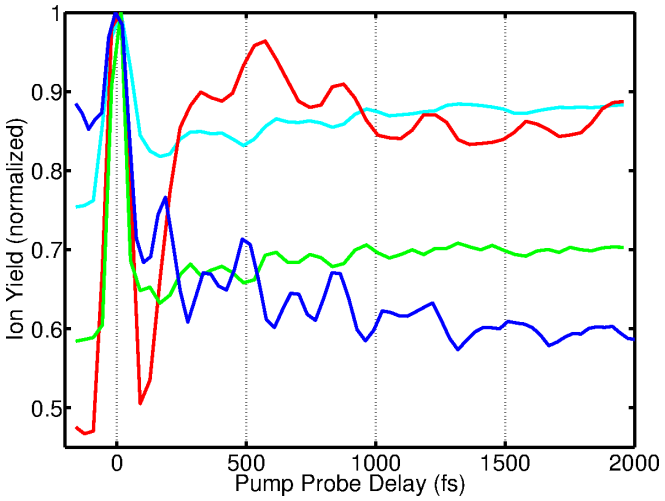

FIG. 5: Ion yields as a function of pump-probe delay. The total CH_2Br^+ and parent ion yields are shown in light blue (upper light gray line) and dark blue (lower dark gray line) respectively. With detailed knowledge of the reconstructed indirect contributions (shown in figure 7) the time behavior of the indirect populations on V_3 and V_4 (leading to CH_2Br^+) can be enhanced. The green (lower gray) curve shows the CH_2Br^+ signal integrated from 0 meV to 400 meV. The red (upper dark gray) curve shows the asymmetric part of the total ion yield for a specific KER interval: $(\int_{400\ meV}^{1.1\ eV} dE\,(Y_p(E,t) - Y_o(E,t))$

ciates and which is the dominant contribution) by the probe as the wave packet crosses FC_2 during evolution on V_1. The evolution of the wavepacket on V_1 can be described theoretically as one-dimensional motion along the bending coordinate [26]. The measured decay time of the oscillations is on the order of several picoseconds. The frequency is measured to be (95 ± 3) cm^{-1} (corresponding to a period of 355fs), in agreement with the previous results [26].

By Fourier transforming the CH_2Br^+ KER signal as a function of time delay and taking the Fourier component corresponding to the vibrational frequency of the wave packet in V_1, we can single out the KER distributions for ions from excited dissociative states of the cation which were populated indirectly via V_1. Figure 6 shows the O and P sector amplitudes and phases for the 95 cm^{-1} Fourier components of the pump probe data: $\widetilde{Y_o}(95\ cm^{-1}, E)$ and $\widetilde{Y_p}(95\ cm^{-1}, E)$ respectively. Here the data was restricted to pump probe delays larger than 200 fs, in order to avoid contributions near zero time delay. The two solid graphs showing the absolute value of the Fourier transform exhibit a clear double peak structure. This becomes even more obvious when looking at the phase associated with each lineout (dashed graphs). The phase is generally flat but jumps from 2.1 rad to about 4.1 rad at about 250 meV KER. While the absolute value of the Fourier transform is determined by amount of population transferred, the phase is determined by the time delay between creating a wavepacket on V_1 (via the pump) and the time of transfer to a dissociative surface (via the probe). Given that there are two peaks in the KER spectrum, and that their phases are different, there must be two separate resonance (FC) positions leading from V_1 to higher lying (dissociative) states of the cation. Since each peak in the KER distribution has a relatively flat phase (outside of the boundary region where the phase changes rapidly with KER), we reconstruct the two underlying KER distributions by taking the amplitude of the spectrum with the two different phases separately. The results are shown in figure 7 along with the KER distribution after excitation with the pump pulse only. We assign these two peaks (slow and fast) to indirect V_4 (and V_3) and indirect V_5 respectively. This assignment is based on three points: First, numerical integration of the the time-dependent Schrödinger equation for the molecule impulsively ionized to V_1 and interacting with a strong probe pulse at intensities comparable to our experimental value predicts transfer of the wave packet from V_1 to V_4 and from V_1 to V_5 via one and three photon coupling with the same phases as observed in the experiment [26]. The wavepacket on V_1 is predicted to move through FC_2 V_1/V_4 twice per round trip (with time offsets of 50 fs and 250 fs), and once per round trip through FC_3 V_1/V_5 with a time delay of 180 fs. Second, the cutoff energies in the reconstructed KERs agree quantitatively with the theoretical estimates -see figure 1. The reconstructed cutoffs are 470 meV and 780 meV for the populations probed to $V_{3,4}$ and V_5 respectively. The predictions based on our calculations are 460 meV ($V_{3,4}$ to channel A) and 910 meV (V_5 to channel D) or 1.01 eV (V_5 to channel C). Finally, the population transferred to V_5 can be distinguished from the population transferred to $V_{3,4}$ by the asymmetry parameter: while the fast peak has an asymmetry value of 0.38, the asymmetry of the slow peak is almost zero - see figure 3. Integrating only over the asymmetric part of the signal $(Y_p(E,t) - Y_o(E,t))$ extracts solely the indirect V_5

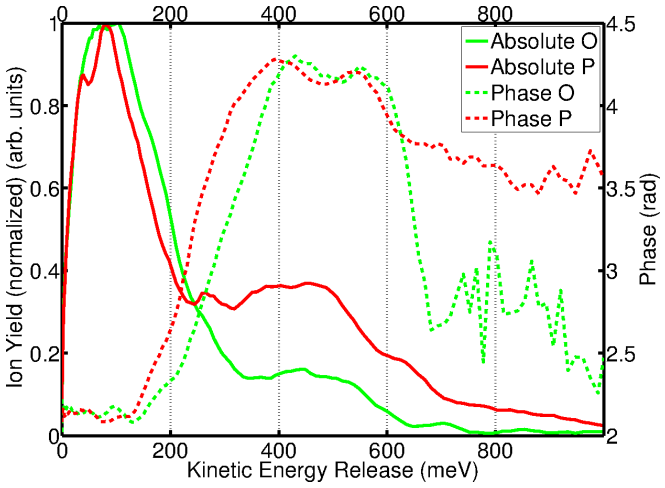

FIG. 6: CH_2Br^+ yield as a function of KER for the Fourier component of the pump probe data at 95 cm^{-1}. This data is the one-dimensional Fourier transform of the data shown in 4 evaluated at 95 cm^{-1}: $\widetilde{Y_{o,p}}(\omega = 95cm^{-1}, E)$. Both sectors (O and P) are analyzed separately. The Fourier transformed signal $\widetilde{Y_{o,p}}(95\ cm^{-1}, E)$ is split into its absolute value (solid lines) and their argument (dashed lines).

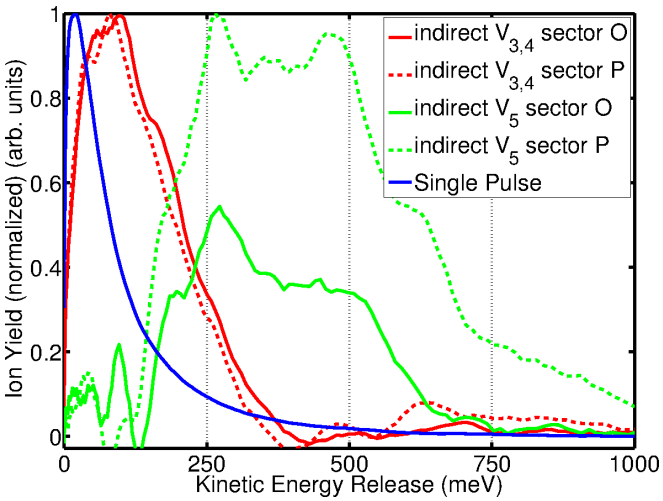

FIG. 7: Reconstructed KER distributions for the indirect $V_{3,4}$ (red/dark gray) and indirect V_5 (green/light gray) population, both sectors are shown individually. The blue/black line shows the KER distribution for a single unshaped pulse for comparison.

contribution. The contrast can be further enhanced by integrating over only the interval from 400 meV to 1.1 eV, where according to figure 7 the indirect V_5 distribution does not overlap with the indirect $V_{3,4}$ distribution. The population probed to $V_{3,4}$ can be extracted by integrating the ion yield only over the region with significant indirect $V_{3,4}$ contribution, but no indirect V_5 contribution; we selected a cutoff of 400 meV. The result of this analysis is shown in figure 5. While the dark/light blue (lower dark gray/upper light gray) signals show the ion yield integrated over KER, the green (lower light gray) and red (upper dark gray) lines highlight the time-dependant behavior of the indirect contributions (i.e. KER selected). The red graph can be described as an oscillation with a frequency of 95 cm^{-1} and total phase offset of 176 fs, the green graph as an oscillation with the same frequency, but two maxima corresponding to phases of 57 fs and 254 fs, in agreement with earlier observations and calculations [26].

C. Chirped Pulse Parameterization

Having identified the part of the CH_2Br^+ KER which comes from indirect population of $V_{3,4}$ with a pump-probe pulse shape paramaterization, we now consider the effect of second-order spectral phase, or chirp on the direct $V_{3,4}$ versus indirect $V_{3,4}$ contributions. Chirping the pulse increases its duration, allowing for nuclear dynamics on V_1 to play a larger role in the total excited state population. In previous work, we showed that it is possible to control the contributions of different ionic states in CH_2I_2 by varying the chirp of the ionization pulse. Figure 8 compares the KER distributions for CH_2Br^+ for two different laser pulses - an unshaped pulse, and a chirped pulse with a group velocity dispersion of -2500 fs^2, which stretches an unshaped pulse to a duration of about 200 fs. The predicted cutoff KER for the direct $V_{3,4}$ population is 310 meV, and indeed the graphs (solid lines) corresponding to a transform-limited pulse show little ion yield beyond this energy range. Ions with more than this energy cannot be generated by direct $V_{3,4}$ ionization, and their number increases by chirping the laser pulse, i.e. positively chirping the pulse shifts the total distributions towards higher KER, with more ions in the fast tail of the peak than for an unshaped laser pulse. Similar effects are observed for negative chirp. On the other hand, it can been seen in figure 7 that the reconstructed KER distribution associated with indirect $V_{3,4}$ is slightly broader and shifted towards higher KER than a single pulse KER (which we expect to be dominated by direct $V_{3,4}$, according to section IV A). This suggests that increasing the pulse duration increases the indirect contributions to $V_{3,4}$ relative to the direct ones.

In order to test our interpretation of the changes in the KER distribution with chirp, we modeled the indirect ionization to $V_{3,4}$ as a function of chirp by following the wave packet evolution on V_1 in the presence of our IR laser pulse as described in the theory section above. We calculated the indirect $V_{3,4}$ population as a function of chirp on the IR laser pulse. The results for the ratio of indirect/direct $V_{3,4}$ populations are shown in figure 9 (dashed curve) [36]. The calculations show that the ratio indirect/direct increases from near zero to above 0.3. Calculations where we kept the nuclei fixed during ionization showed no change in the indirect/direct ratio, indicating that evolution of the nuclear wave packet on

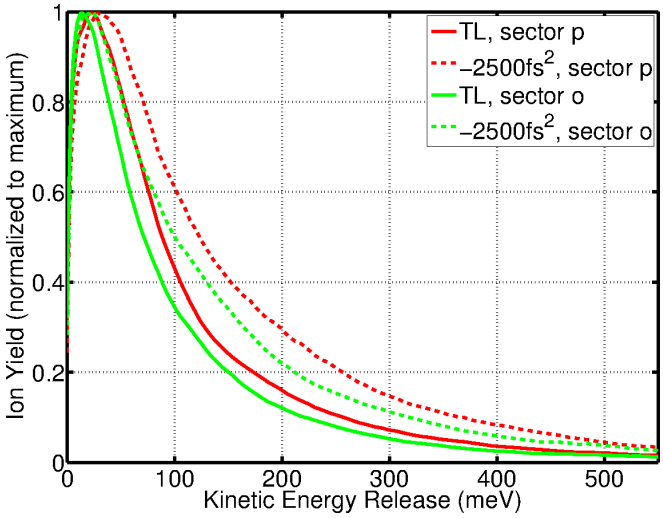

FIG. 8: KER distributions for CH_2Br^+ (showing the slow peak only). The distributions are shown for the orthogonal and the parallel sectors separately. The graph compares the distributions for excitation with an unshaped pulse versus a strongly chirped pulse. All graphs have been normalized to the maximum ion yield.

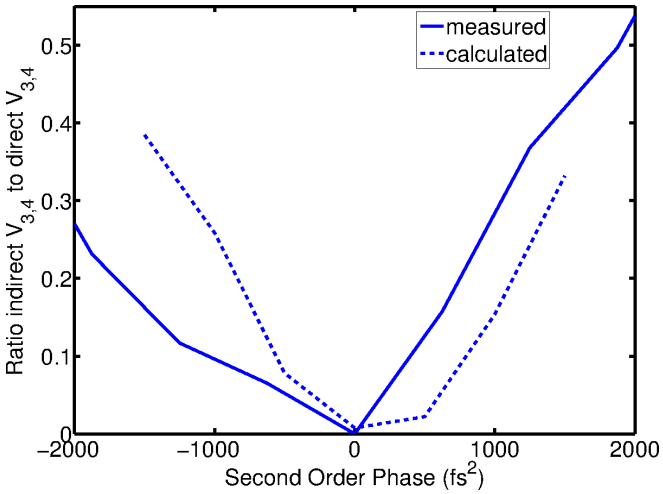

FIG. 9: Dependence of KER distribution of the slow peak on chirp. The dashed graph shows the calculated ratio "indirect $V_{3,4}$" / "direct $V_{3,4}$" population versus chirp. The solid graph shows the ratio extracted from our measurements by using the reconstructed direct and indirect $V_{3,4}$ and indirect V_5 distributions as a basis set.

V_1 is a key part of the indirect transfer.

The KER distributions interpreted in the previous section can be used to extract chirp dependent direct and indirect $V_{3,4}$ yields, and compare their ratio with the simulation. We fitted the measured KER distribution for each chirp with a basis set formed by the reconstructed indirect $V_{3,4}$ distribution, the indirect V_5 distribution, and the KER distribution associated with a low intensity unshaped pulse, consisting of mostly direct $V_{3,4}$ ions [37]. These three basis vectors allow us to generate the entire observed KER distribution, with an error of less than 5%. The result is shown in the solid curve in figure 9. Both experiments and calculations agree qualitatively, showing a similar trend of increasing indirect/direct ratio as a function of pulse chirp. We note that the measurements show a different asymmetry with chirp than the calculations. This suggests that there are some subtleties in the ionization process that are not captured by our calculations, which treat the coupling between the neutral and ionic states in a simple manner. This is consistent with our earlier measurements on CH_2I_2, which showed asymmetric chirp dependence in the ionization to different cationic states [10]. We also note that our interpretation of the experimental data assumes that the KER distributions associated with the various populations do not change significantly with laser pulse shape. In particular, the reconstructed indirect KER distributions used as a basis here are based on pump probe data, where the wavepacket propagated on the adiabatic V_1 state. However, in the case of indirect ionization to V_4 via a chirped pulse, the population temporarily evolves on a dressed (or dynamically Stark shifted) potential energy surfaces during ionization. Stark shifts could account for KERs above 310 meV associated with direct ionization to $V_{3,4}$ (where the fit would assign it to the distributions of the indirect populations), thus leading to a slight overestimation of the indirect $V_{3,4}$ populations.

V. CONCLUSION

In conclusion, we have studied the strong field ionization of CH_2BrI with velocity map imaging and found multiple pathways to dissociative states of the molecular cation. The KER spectrum and angular distributions for different pulse shapes, in conjunction with *ab initio* electronic structure calculations and integration of the time-dependent Schrödinger equation helped to identify which states are populated via specific pathways. We note that the reconstructed distributions could in principle be used as a basis set to fit the KER distributions after excitation with any arbitrary pulse shape, thus creating a direct relation between excitation pulse shape and populations of electronic states.

We gratefully acknowledge support from the National Science Foundation under Award number 0854922, the Hungarian Academy of Sciences and Deutsche Forschungsgemeninschaft (Nr. 436 UNG 113/188/0-1), and the European COST Action CM0702.

[1] J. Itatani, J. Levesque, D. Zeidler, H. Niikura, H. Pepin, J. Kieffer, P. Corkum, and D. Villeneuve, Nature **432**, 867 (2004).

[2] S. Haessler, J. Caillat, W. Boutu, C. Giovanetti-Teixeira, T. Ruchon, T. Auguste, Z. Diveki, P. Breger, A. Maquet, B. Carré, et al., Nat. Phys **6**, 200 (2010).

[3] F. Krausz and M. Ivanov, Rev. Mod. Phys. **81**, 163 (2009).

[4] M. Kling and M. Vrakking, Annu. Rev. Phys. Chem. **59**, 463 (2008).

[5] P. Agostini and L. DiMauro, Reports on Progress in Physics **67**, 813 (2004).

[6] L. Dimauro and P. Agostini (Academic Press, 1995), vol. 35 of *Advances In Atomic, Molecular, and Optical Physics*, pp. 79 – 120.

[7] C. F. d. M. Faria and X. Liu, Journal of Modern Optics **58**, 1076 (2011).

[8] M. Spanner and S. Patchkovskii, Phys. Rev. A **80**, 063411 (2009).

[9] L. Fang and G. N. Gibson, Phys. Rev. A **75**, 063410 (2007).

[10] D. Geißler, T. Rozgonyi, J. González-Vázquez, L. González, S. Nichols, and T. Weinacht, Phys. Rev. A **82** (2010).

[11] C. Wu, H. Zhang, H. Yang, Q. Gong, D. Song, and H. Su, Phys. Rev. A **83**, 033410 (2011).

[12] G. N. Gibson, R. R. Freeman, and T. J. McIlrath, Phys. Rev. Lett. **67**, 1230 (1991).

[13] H. Akagi et al., Science **325**, 1364 (2009).

[14] O. Smirnova et al., Nature **460**, 972 (2009).

[15] B. K. Mc Farland, J. P. Farrell, P. H. Bucksbaum, and M. Guhr, Science **322**, 1232 (2008).

[16] H. J. Wörner, J. B. Bertrand, P. Hockett, P. B. Corkum, and D. M. Villeneuve, Phys. Rev. Lett. **104**, 233904 (2010).

[17] F. Langhojer, D. Cardoza, M. Baertschy, and T. Weinacht, The Journal of Chemical Physics **122**, 014102 (pages 10) (2005).

[18] M. A. Dugan, J. X. Tull, and W. S. Warren, J. Opt. Soc. Amer. B **14**, 2348 (1997).

[19] A. T. J. B. Eppink and D. H. Parker, **68**, 3477 (1997).

[20] D. A. Dahl, International Journal of Mass Spectrometry **200**, 325 (2000).

[21] *Gaussian 2003*, M. Frisch, et al., Gaussian Inc., Wallingford, CT (2003).

[22] W. Y. C.Lee and R. Parr, Phys. Rev. B **37**, 785 (1988).

[23] A. Becke, J. Chem. Phys. **98**, 5648 (1993).

[24] K. A. Peterson et al., J. Chem. Phys. **119**, 11113 (2003).

[25] S. R. Nichols, T. C. Weinacht, T. Rozgonyi, and B. J. Pearson, Phys. Rev. A **79**, 043407 (2009).

[26] J. González-Vázquez, L. González, S. R. Nichols, T. C. Weinacht, and T. Rozgonyi, Phys. Chem. Chem. Phys. **12**, 14203 (2010).

[27] B. O. Roos, P. R. Taylor, and P. E. M. Siegbahn, Chemical Physics **48**, 157 (1980), ISSN 0301-0104.

[28] F. Aquilante, L. De Vico, N. Ferré, G. Ghigo, P.-r. Malmqvist, P. Neogrády, T. B. Pedersen, M. Pitoňák, M. Reiher, B. O. Roos, et al., J. Comput. Chem. **31**, 224 (2010).

[29] H.-J. Werner, P. J. Knowles, G. Knizia, F. R. Manby, M. Schütz, et al., *Molpro, version 2010.1, a package of ab initio programs* (2010).

[30] B. A. Heß, C. M. Marian, U. Wahlgren, and O. Gropen, Chemical Physics Letters **251**, 365 (1996), ISSN 0009-2614.

[31] B. Schimmelpfennig, *AMFI, an atomic mean field spin-orbit program* (1996).

[32] P.-O. Widmark et al., Theor. Chim. Acta **77** (1990).

[33] B. Roos et al., J. Phys. Chem. A **108**, 2851 (2004).

[34] A. F. Lago, J. P. Kercher, A. Bdi, B. Sztray, B. Miller, D. Wurzelmann, and T. Baer, The Journal of Physical Chemistry A **109**, 1802 (2005).

[35] L. Minnhagen, Ark. Fys. **21**, 415 (1962).

[36] For the calculated ratio we show the indirect population for each chirp divided by the direct population at a fixed (zero) chirp. We believe that this provides a more realistic estimate of the measured ratio than the indirect population for each chirp divided by the direct population for each chirp given the limitations of our model.

[37] We note that for relatively high intensities ($\sim 4{\cdot}10^{13}$ W cm^{-2}), the slow peak shifts slightly to higher KER (as seen in figure 3 compared to 8), consistent with some additional indirect $V_{3,4}$ population. At higher intensities, ionization to V_1 can occur earlier than for lower intensities and successive transfer to V_4 can occur more readily as there is more intensity in the tail of the pulse to drive the V_1 to V_4 transition.